Deep learning and the Schrödinger equation

Kyle Mills[*]

Department of Physics, University of Ontario Institute of Technology, Oshawa, Ontario, Canada L1H 7K4

Michael Spanner

National Research Council of Canada, Ottawa, Ontario, Canada K1A 0R6

Isaac Tamblyn[†]

Department of Physics, University of Ontario Institute of Technology, Oshawa, Ontario, Canada L1H 7K4
and National Research Council of Canada, Ottawa, Ontario, Canada K1A 0R6

We have trained a deep (convolutional) neural network to predict the ground-state energy of an electron in four classes of confining two-dimensional electrostatic potentials. On randomly generated potentials, for which there is no analytic form for either the potential or the ground-state energy, the model was able to predict the ground-state energy to within chemical accuracy, with a median absolute error of 1.49 mHa. We also investigated the performance of the model in predicting other quantities such as the kinetic energy and the first excited-state energy.

I. INTRODUCTION

Solving the electronic structure problem for molecules, materials, and interfaces is of fundamental importance to a large number of disciplines including physics, chemistry, and materials science. Since the early development of quantum mechanics, it has been noted, by Dirac among others, that "...approximate, practical methods of applying quantum mechanics should be developed, which can lead to an explanation of the main features of complex atomic systems without too much computation" [1]. Historically, this has meant invoking approximate forms of the underlying interactions (mean field, tight binding, etc.) or relying on phenomenological fits to a limited number of either experimental observations or theoretical results (e.g., force fields) [2–8]. The development of feature-based models is not new in the scientific literature. Indeed, prior even to the acceptance of the atomic hypothesis, van der Waals argued for an equation of state based on two physical features [9]. Machine learning (i.e., fitting parameters within a model) has been used in physics and chemistry since the dawn of the computer age. The term machine learning is new; the approach is not.

More recently, high-level *ab initio* calculations have been used to train artificial neural networks to fit high-dimensional interaction models [10–15] and to make informed predictions about material properties [16,17]. These approaches have proven to be quite powerful, yielding models trained for specific atomic species or based upon hand-selected geometric features [18–20]. Hand-selected features are arguably a significant limitation of such approaches, with the outcomes dependent upon the choice of input representation and the inclusion of all relevant features. This limitation is well known in the fields of handwriting recognition and image classification, where the performance of the traditional hand-selected feature approach has stagnated [21].

Such feature-based approaches are also being used in materials discovery [22–24] to assist materials scientists in efficiently targeting promising material candidates. Unsupervised learning techniques have been used to identify phases in many-body atomic configurations [25]. In previous work, an artificial neural network was shown to interpolate the mapping of position to wave function for a specific electrostatic potential [26–28], but the fit was not transferable, a limitation also present in other applications of artificial neural networks to partial differential equations [29,30]. By transferable, we mean that a model trained on a particular form of partial differential equation will accurately and reliably predict results for examples of the same form (in our case, different confining potentials).

Machine learning can also be used to accelerate or bypass some of the heavy machinery of the *ab initio* method itself. In [31], the authors replaced the kinetic energy functional within density-functional theory with a machine-learned one, and in [32,33], the authors "learned" the mappings from potential to electron density and from charge density to kinetic energy, respectively.

Here we use a fundamentally different approach inspired by the successful application of deep convolutional neural networks to problems in computer vision [34–37] and computational games [38,39]. Rather than seeking an appropriate input representation to capture the relevant physical attributes of a system, we train a highly flexible model on an enormous collection of ground-truth examples. In doing so, the deep neural network learns both the features (in weight space) and the mapping required to produce the desired output. This approach does not depend on the appropriate selection of input representations and features; we provide the same data to both the deep neural network and the numerical method. As such, we call this featureless learning. Such an approach may offer a more scalable and parallelizable approach to large-scale electronic structure problems than existing methods can offer.

[*]kyle.mills@uoit.net
[†]isaac.tamblyn@nrc.ca

In this paper we demonstrate the success of a featureless machine learning approach, a convolutional deep neural network, at learning the mapping between a confining electrostatic potential and quantities such as the ground-state energy, kinetic energy, and first excited state of a bound electron. The excellent performance of our model suggests deep learning as an important direction for treating multielectron systems in materials.

It is known that a sufficiently large artificial neural network can approximate any continuous mapping [40,41], but the cost of optimizing such a network can be prohibitive. Convolutional neural networks make computation feasible by exploiting the spatial structure of input data [42], similar to how the neurons in the visual cortex function [43]. When multiple convolutional layers are included, the network is called a deep convolutional neural network, forming a hierarchy of feature detection [44]. This makes them particularly well suited to data rooted in physical origin [45,46], since many physical systems also display a structural hierarchy. Applications of such a network structure in the field of electronic structure, however, are few (although recent work focused on training against a geometric matrix representation looks particularly promising [47]).

II. METHODS

A. Training set: Choice of potentials

Developing a deep learning model involves both the design of the network architecture and the acquisition of training data. The latter is the most important aspect of a machine learning model, as it defines the transferability of the resulting model. We investigated four classes of potentials: simple harmonic oscillators (SHOs), infinite wells (IWs) (i.e., particle in a box), double-well inverted Gaussians (DIG), and random potentials. Each potential can be thought of as a grayscale image: a grid of floating-point numbers.

B. Numerical solver

We implemented a standard finite-difference [48] method to solve the eigenvalue problem

$$\hat{H}\psi \equiv (\hat{T} + \hat{V})\psi = \varepsilon\psi \tag{1}$$

for each potential V we created. The potentials were generated with a dynamic range and length scale suitable to produce ground-state energies within a physically relevant range. With the random potentials, special care was taken to ensure that some training examples produced nontrivial wave functions (Fig. 1). Atomic units are used, such that $\hbar = m_e = 1$. The potentials are represented on a square domain from -20 to 20 a.u., discretized on a 256×256 grid. As the simple-harmonic-oscillator potentials have an analytic solution, we used this as reference with which to validate the accuracy of the solver. The median absolute error between the analytic and the calculated energies for all simple-harmonic-oscillator potentials was 0.12 mHa. We discuss the generation of all potentials further in the Appendixes.

The simple harmonic oscillator presents the simplest case for a convolutional neural network as there is an analytic solution dependent on two simple parameters (k_x and k_y) that
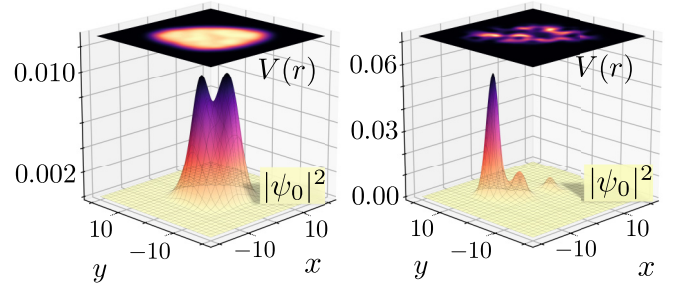

FIG. 1. Wave functions (probability density) $|\psi_0|^2$ and the corresponding potentials $V(r)$ for two random potentials.

uniquely define the ground-state energy of a single electron [$\varepsilon_0 = \frac{\hbar}{2}(\sqrt{k_x} + \sqrt{k_y})$]. Furthermore, these parameters represent a very physical and visible quantity: the curvature of the potential in the two primary axes. Although these parameters are not provided to the neural network explicitly, the fact that a simple mapping exists means that the convolutional neural network need only learn it to accurately predict energies.

A similar situation exists for the infinite well. Like the simple harmonic oscillator, the ground-state energy depends only on the width of the well in the two dimensions [$\varepsilon_0 = \frac{1}{2}\pi^2\hbar^2(L_x^{-2} + L_y^{-2})$]. It would be no surprise if even a modest network architecture is able to accurately "discover" this mapping. An untrained human, given a ruler, sufficient examples, and an abundance of time, would likely succeed in determining this mapping.

The double-well inverted Gaussian data set is more complex in two respects. First, the potential, generated by summing a pair of two-dimensional (2D) Gaussians, depends on significantly more parameters; the depth, width, and aspect ratio of each Gaussian; in addition, the relative positions of the wells will impact the ground-state energy. Furthermore, there is no known analytical solution for a single electron in a potential well of this nature. There is, however, still a concise function that describes the underlying potential, and while this is not directly accessible to the convolutional neural network, one must wonder if the existence of such simplifies the task of the convolutional neural network. Gaussian confining potentials appear in works relating to quantum dots [49,50].

The random data set presents the ultimate challenge. Each random potential is generated by a multistep process with randomness introduced at numerous steps along the way. There is no closed-form equation to represent the potentials and certainly not the eigenenergies. A convolutional neural network tasked with learning the solution to the Schrödinger equation through these examples would have to base its predictions on many individual features, truly learning the mapping of potential to energy. One might question our omission of the Coulomb potential as an additional canonical example. The singular nature of the Coulomb potential is difficult to represent within a finite dynamic range and, more importantly, the electronic structure methods that we would ultimately seek to reproduce already have frameworks in place to deal with these singularities (e.g., pseudopotentials).
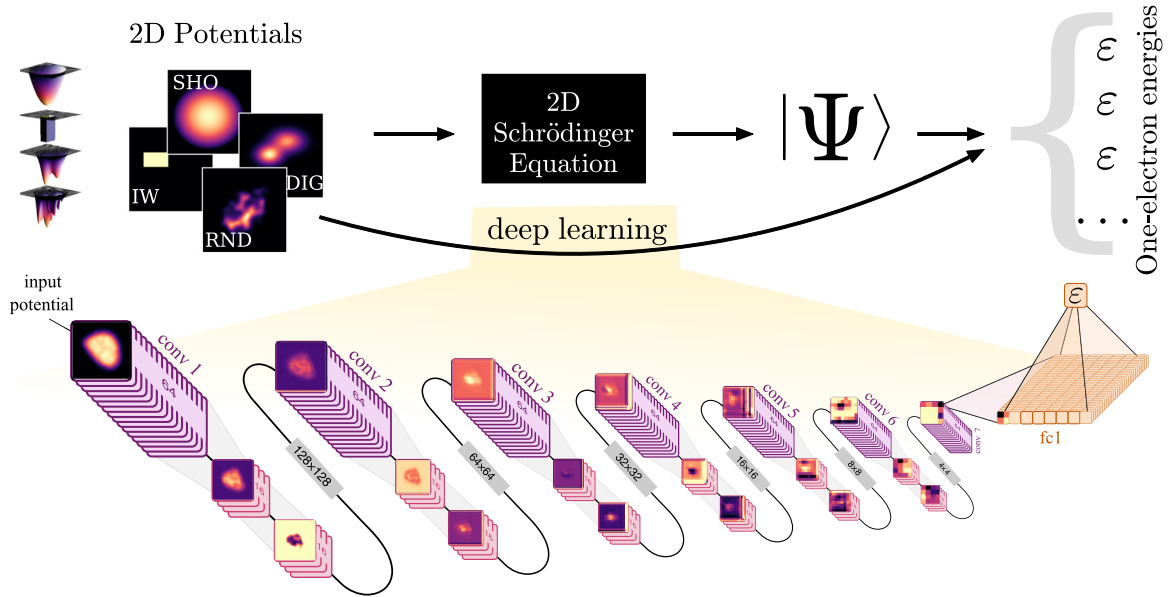
FIG. 2. In this work, we use the machinery of deep learning to learn the mapping between potential and energy, bypassing the need to numerically solve the Schrödinger equation and the need for computing wave functions. The architecture we used (shown here) consisted primarily of convolutional layers capable of extracting relevant features of the input potentials. Two fully connected layers at the end serve as a decision layer, mapping the automatically extracted features to the desired output quantity. No manual feature selection is necessary; this is a featureless-learning approach.

C. Deep neural network

We chose to use a simple yet deep neural network architecture (shown in Fig. 2) composed of a number of repeated units of convolutional layers, with sizes chosen for a balance of speed and accuracy (inset of Fig. 3). We use two different types of convolutional layers, which we call reducing and nonreducing.

The seven reducing layers operate with filter (kernel) sizes of 3×3 pixels. Each reducing layer operates with 64 filters and a stride of 2×2, effectively reducing the image resolution
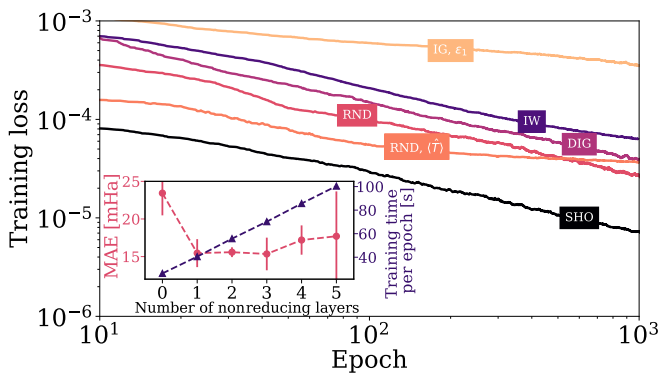

FIG. 3. Training loss curve for each model we trained. Since the training loss is based upon the training data sets, it does not necessarily indicate how well the model generalizes to new examples. The convergence seen here indicates that 1000 epochs is an adequate stopping point; further training would produce further reduction in loss, however 1000 epochs provides sufficient evidence that the method performs well on the most interesting (i.e., random) potentials. In the inset, we see that two nonreducing convolution layers is a consistent balance of training time and low error.

by a factor of 2 at each step. In between each pair of these reducing convolutional layers, we have inserted two convolutional layers (for a total of 12) that operate with 16 filters of size 4×4. These filters have unit stride and therefore preserve the resolution of the image. The purpose of these layers is to add additional trainable parameters to the network. All convolutional layers have rectified linear unit (ReLU) activation.

The final convolutional layer is fed into a fully connected layer of width 1024, also with ReLU activation. This layer feeds into a final fully connected layer with a single output. This output is the output value of the deep neural network (DNN). It is used to compute the mean-square error between the true label and the predicted label, also known as the loss.

We used the AdaDelta [51] optimization scheme with a global learning rate of 0.001 to minimize this loss function (Fig. 3), monitoring its value as training proceeded. We found that after 1000 epochs (1000 times through all the training examples), the loss no longer decreased significantly.

We built a custom TensorFlow [52] implementation in order to make use of four graphical processing units (GPUs) in parallel. We placed a complete copy of the neural network on each of the four GPUs, so that each could compute a forward- and backpropagation iteration on one full batch of images. Thus our effective batch size was 1000 images per iteration (250 per GPU). After each iteration, the GPUs share their independently computed gradients with the optimizer and the optimizer moves the parameters in the direction that minimizes the loss function. Unless otherwise specified, all training data sets consisted of 200 000 training examples and training was run for 1000 epochs. All reported errors are based on evaluating the trained model on validation data sets consisting of 50 000 potentials not accessible to the network during the training process.
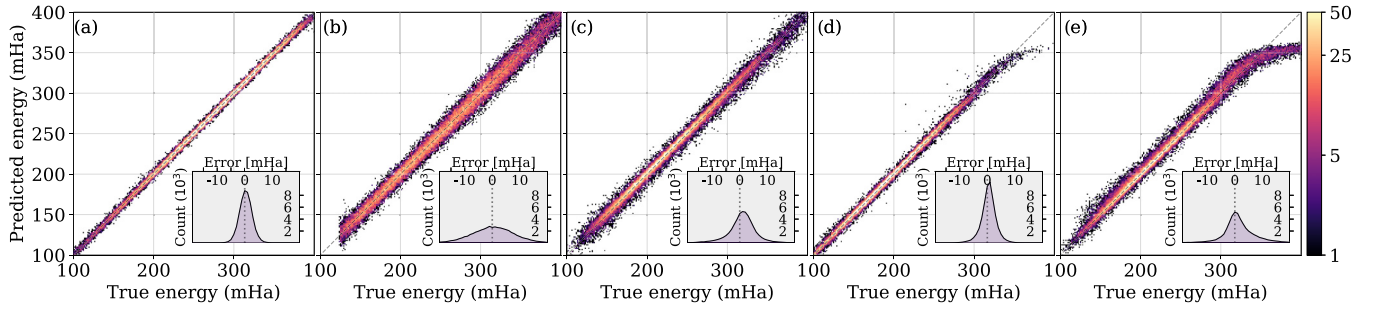
FIG. 4. Histograms of the true vs predicted energies for each example in the test set indicate the performance of the various models: (a) simple harmonic oscillator, (b) infinite well, (c) DIG potential, (d) random potential, and (e) DIG potential on random model. The insets show the distribution of error away from the diagonal line representing perfect predictions. A 1-mHa^2 square bin is used for the main histograms and a 1-mHa bin size for the inset histogram. During training, the neural network was not exposed to the examples on which theses plots are based. The higher error at high energies in (d) is due to fewer training examples being present in the data set at these energies. The histogram shown in (d) is for the further-trained model, described in the text.

III. RESULTS

Figures 4(a)–4(d) displays the results for the simple-harmonic-oscillator, infinite well, double-well inverted Gaussian, and random potentials. The simple harmonic oscillator, being one of the simplest potentials, performed extremely well. The trained model was able to predict the ground-state energies with a median absolute error (MAE) of 1.51 mHa.

The infinite well potentials performed moderately well with a MAE of 5.04 mHa. This is notably poorer than the simple-harmonic-oscillator potentials, despite their similarity in being analytically dependent upon two simple parameters. This is likely due to the sharp discontinuity associated with the infinite well potentials, combined with the sparsity of information present in the binary-valued potentials.

The model trained on the double-well inverted Gaussian potentials performed moderately well with a MAE of 2.70 mHa and the random potentials performed quite well with a MAE of 2.13 mHa. We noticed, however, that the loss was not completely converged at 1000 epochs, so we provided an additional 200 000 training examples to the network and allowed it to train for an additional 1000 epochs. With this added training, the model performed exceptionally well, with a MAE of 1.49 mHa, below the threshold of chemical accuracy (1 kcal/mol, 1.6 mHa). In Fig. 4(d), it is evident that the model performs more poorly at high energies, a result of the relative absence of high-energy training examples in the data set. Given the great diversity in this latter set of potentials, it is impressive that the convolutional neural network was able to learn how to predict the energy with such a high degree of accuracy.

Now that we have a trained model that performs well on the random test set, we investigated its transferability to another class of potentials. The model trained on the random data set is able to predict the ground-state energy of the double-well inverted Gaussian potentials with a MAE of 2.94 mHa. We can see in Fig. 4(e) that the model fails at high energies, an expected result given that the model was not exposed to many examples in this energy regime during training on the overall lower-energy random data set. This moderately good performance is not entirely surprising; the production of the random potentials includes an element of Gaussian blurring, so the neural network would have been exposed to features similar

to what it would see in the double-well inverted Gaussian data set. However, this moderate performance is a testament to the transferability of convolutional neural network models. Furthermore, we trained a model on an equal mixture of all four classes of potentials. It performs moderately with a MAE of 5.90 mHa. This error could be reduced through further tuning of the network architecture, allowing it to better capture the higher variation in the data set.

The total energy is just one of the many quantities associated with these one-electron systems. To demonstrate the applicability of deep neural networks to other quantities, we trained a model on the first excited-state energy ε_1 of the double-well inverted Gaussian potentials. The model achieved a MAE of 10.93 mHa. We now have two models capable of predicting the ground-state and first-excited-state energies separately, demonstrating that a neural network can learn quantities other than the ground-state energy.

The ground-state and first excited state are both eigenvalues of the Hamiltonian. Therefore, we investigated the training of a model on the expectation value of the kinetic energy $\langle \hat{T} \rangle = \langle \psi_0 | \hat{T} | \psi_0 \rangle$ under the ground-state wave function ψ_0 that we computed numerically for the random potentials. Since $\hat{H}$ and $\hat{T}$ do not commute, the prediction of $\langle \hat{T} \rangle$ can no longer be summarized as an eigenvalue problem. The trained model predicts the kinetic energy value with a MAE of 2.98 mHa. While the spread of testing examples in Fig. 5(a) suggests that the model performs more poorly, the absolute error is still small.
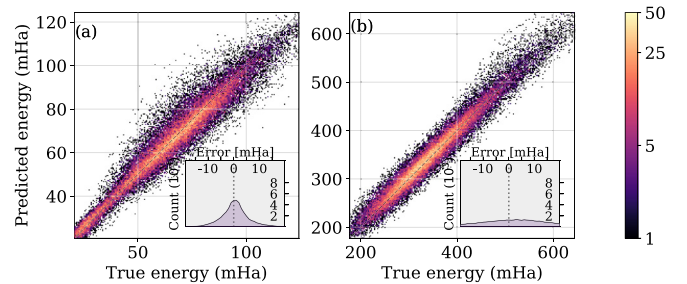

FIG. 5. Histograms of the true vs predicted energies for the model trained on the (a) kinetic energy $\langle \hat{T} \rangle$ of the random potential and (b) excited-state energy ε_1 of the double-well inverted Gaussian.

IV. CONCLUSION

We note that many other machine learning algorithms exist and have traditionally seen great success, such as kernel ridge regression [18,20,32,53–55] and random forests [18,56]. Like these algorithms, convolutional deep neural networks have the ability to learn relevant features and form a nonlinear input-to-output mapping without prior formulation of an input representation [47,57]. In our tests, these methods performed more poorly and scaled such that a large number of training examples is infeasible. We have included a comparison of these alternative machine learning methods in the Appendixes, justifying our decision of using a deep convolutional neural network. One notable limitation of our approach is that the efficient training and evaluation of the deep neural network requires uniformity in the input size. Future work should focus on an approach that would allow transferability to variable input sizes.

Additionally, an electrostatic potential defined on a finite grid can be rotated in integer multiples of $90°$, without a change to the electrostatic energies. Convolutional deep neural networks do not natively capture such rotational invariance. Clearly, this is a problem in any application of deep neural networks (e.g., image classification) and various techniques are used to compensate for the desired invariance. The common approach is to train the network on an augmented data set consisting of both the original training set and rotated copies of the training data [58]. In this way, the network learns a rotationally invariant set of features.

In demonstration of this technique, we tuned our model trained on the random potentials by training it further on an augmented data set of rotated random potentials. We then tested our model on the original testing data set as well as a rotated copy of the test set. The median absolute error in both cases was less than 1.6 mHa. The median absolute difference in predicted energy between the rotated and unaltered test sets was however larger, at 1.7 mHa. This approach to training the deep neural network is not absolutely rotationally invariant, however the numerical error experienced due to a rotation was on the same order as the error of the method itself. Recent proposals to modify the network architecture itself to make it rotationally invariant are promising, as the additional training cost incurred with using an augmented data set could be avoided [59,60].

In summary, convolutional deep neural networks are promising candidates for application to electronic structure calculations as they are designed for data that have a spatial encoding of information. As the number of electrons in a system increases, the computational complexity grows polynomially. Accurate electronic structure methods (e.g., coupled cluster) exhibit a scaling with respect to the number of particles of N^7 and even the popular Kohn-Sham formalism of density-functional theory scales as N^3 [61,62]. The evaluation of a convolutional neural network exhibits no such scaling, and while the training process for more complicated systems would be more expensive, this is a one-time cost.

In this work we have taken a simple problem (one electron in a confining potential) and demonstrated that a convolutional neural network can automatically extract features and learn the mapping between $V(r)$ and the ground-state energy ε_0 as well as the kinetic energy $\langle \hat{T} \rangle$, and the first-excited-state energy ε_1. Although our focus here has been on a particular type of problem, namely, an electron in a confining 2D well, the concepts here are directly applicable to many problems in physics and engineering. Ultimately, we have demonstrated the ability of a deep neural network to learn, through example alone, how to rapidly approximate the solution to a set of partial differential equations. A generalizable, transferable deep learning approach to solving partial differential equations would impact all fields of theoretical physics and mathematics.

APPENDIX A: COMPARISON OF MACHINE LEARNING METHODS

One might question the use of a convolutional deep neural network over other more traditional machine learning approaches. After all, kernel ridge regression (KRR), random forests (RF), and artificial neural networks (ANN) have proven to be quite useful (see the main text for references to appropriate work). Here we compare the use of our convolutional deep neural network approach to kernel ridge regression and random forests, the latter two implemented through Scikit-learn [63].

1. Kernel ridge regression

We trained a kernel ridge regression model on a training set of simple-harmonic-oscillator images, recording the wall time
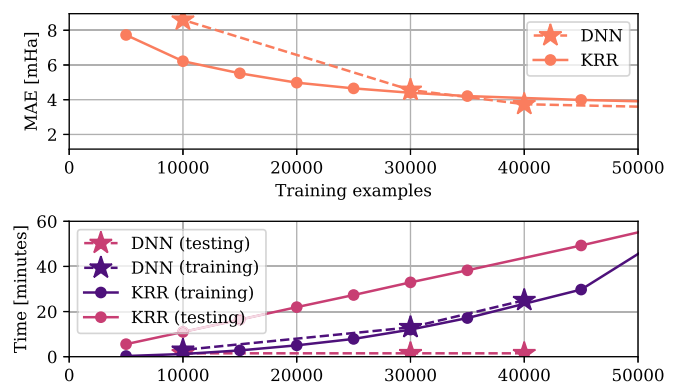

FIG. 6. Kernel ridge regression on simple-harmonic-oscillator potentials. When few training examples are provided, kernel ridge regression performs better; however, with a larger number of training examples, both methods perform comparably, with DNN slightly better. The training time for kernel ridge regression scales quadratically. The evaluation time for a fixed number of testing examples scales linearly with respect to the number of training examples in the case of kernel ridge regression. In the case of the deep neural network, the training set size does not affect the testing set evaluation.
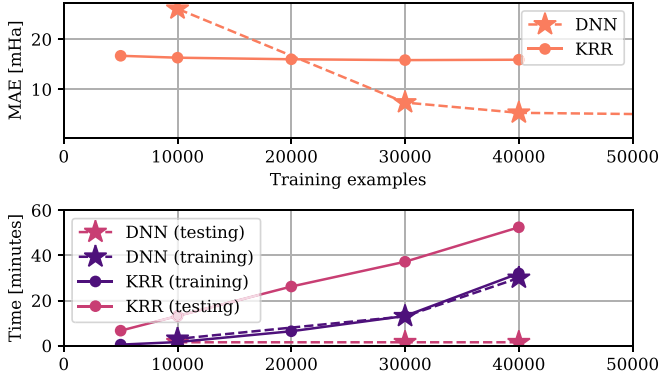
FIG. 7. Kernel ridge regression on random potentials. When few training examples are present, kernel ridge regression performs better (at constant training time). This is likely due to the fact that the DNN is only given 10 s to run. At larger training set sizes, the deep neural network performs much better; kernel ridge regression barely improves as training set size increases, however training wall time increases dramatically.

(real-world time) taken to train the model. Then we evaluated the trained model on a test set (the same test set was used throughout). We recorded both the evaluation wall time and the MAE observed from the trained model. We then trained our deep neural network on the same training data set, allowing it the same training wall time as the KRR model. We then evaluated the deep neural network on the same testing set of data, again recording the MAE and the evaluation wall time. This process was repeated for various training set sizes and on training data from both the simple-harmonic-oscillator and random data sets. The results are presented in Figs. 6 and 7.

2. Random forests

We carried out an identical process, training a random forests regressor. The results are presented in Figs. 8 and 9.
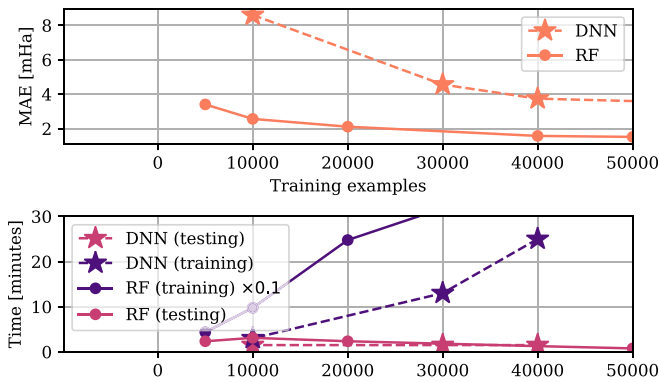

FIG. 8. Random forests on simple harmonic oscillator. Random forests perform better than deep neural networks for all training set sizes on the relatively trivial simple-harmonic-oscillator data set. Random forests takes a very long time to train. Note that the training times plotted above have been scaled by a factor of 0.1 for plotting and thus the true times are ten times greater than shown.
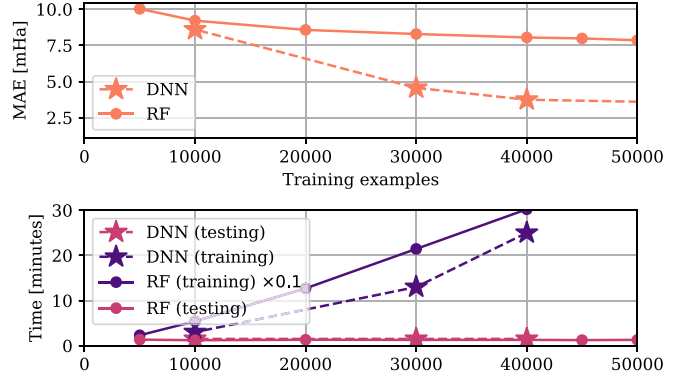

FIG. 9. Random forests on random potentials. On the more complicated random potentials, random forests perform significantly worse than the deep neural network. This combined with the extremely high training time suggests that the deep neural network is much better equipped to handle these more varied potentials.

3. Discussion

While the timing comparison is not quantitatively fair (the random forest algorithm is not parallelized and uses only one CPU core, the kernel ridge regression algorithm is parallelized and ran across all available cores, and the deep neural network is highly parallelized via GPU optimization and runs across thousands of cores), this investigation gives useful insight into the time-to-solution advantages of deep neural networks. The error rates, however are quantitatively comparable, as the KRR and random forest (RF) algorithms were permitted to run until convergence. The DNN was able to perform better in most cases given the same amount of wall time.

We see that for all but the simplest cases, our deep neural network is vastly superior to both kernel ridge regression and random forests. For very simple potentials, it is understandable that the machinery of the deep neural network was unnecessary and that the traditional methods perform well. For more complicated potentials with more variation in the input data, the deep neural network was able to provide significantly better accuracy in the same amount of time.

APPENDIX B: DATA-SET GENERATION

The potentials are defined on a grid from $x, y = -20$ to 20 a.u. on a 256×256 grid.

1. Simple harmonic oscillator

The SHO potentials are generated with the scalar function

$$V(x, y) = \tfrac{1}{2}[k_x(x - c_x)^2 + k_y(y - c_y)^2], \tag{B1}$$

TABLE I. Random number generation criteria for the simple-harmonic-oscillator dataset.

Parameter	Description	Lower bound	Upper bound
k_x	spring constant	0.0	0.16
k_y	spring constant	0.0	0.16
c_x	center position	−8.0	8.0
c_y	center position	−8.0	8.0

TABLE II. Random number generation criteria for the double-well-inverted-Gaussian dataset.

Parameter	Description	Lower bound	Upper bound
A_1	well 1 depth	2.0	4.0
A_2	well 2 depth	2.0	4.0
c_{x_1}	well 1 center x	-8.0	8.0
c_{y_1}	well 1 center y	-8.0	8.0
c_{x_2}	well 2 center x	-8.0	8.0
c_{y_2}	well 2 center y	-8.0	8.0
k_{x_1}	well 1 width	1.6	8.0
k_{y_1}	well 1 length	1.6	8.0
k_{x_2}	well 2 width	1.6	8.0
k_{y_2}	well 2 length	1.6	8.0

where k_x, k_y, c_x, and c_y are randomly generated according to Table I. The potentials are truncated at 20.0 Ha (i.e., if $V > 20$, $V = 20$).

2. Infinite well

The IW potentials are generated with the scalar function

$$V(x,y) = \begin{cases} 0 & \frac{1}{2}(2c_x - L_x) < x \leqslant \frac{1}{2}(2c_x + L_x), \\ & \frac{1}{2}(2c_y - L_y) < y \leqslant \frac{1}{2}(2c_y + L_y) \\ 20 & \text{otherwise,} \end{cases} \quad \text{(B2)}$$

where 20.0 is used as numerical infinity, an appropriate choice given the scale of energies used. Because of the nature of the IW energy, randomly generating L_x and L_y independently leads to a distribution of energies highly biased toward low-energy values (it is more likely to randomly produce a large well than a small). Since we want a distribution that is as even as possible over the range of energies, we need to take a slightly different approach. We randomly generate the energy E uniformly on the interval [0,0.4] Ha. We then generate L_x randomly on the interval [4.0,15.0], defining the width of the well. We then solve for the value of L_y that will produce an energy of E, given L_x, e.g.,

$$L_y = 1 \Big/ \sqrt{\frac{2E}{\pi^2} - \frac{1}{L_x^2}}. \quad \text{(B3)}$$

Not all combinations of L_x and E lead to valid solutions for L_y, so we keep trying until one does. We then swap the values of L_x and L_y with a 50% probability to prevent one dimension of the well always being larger. This process leads to a relatively even distribution of energies.

TABLE III. Random number generation criteria for the random potential dataset. In column 2, SD denotes standard deviation.

Parameter	Description	Lower bound	Upper bound
σ_1	SD blur 1	6	10
k	blob points	2	7
R	blob size	80	180
σ_2	SD blur 2	10	16
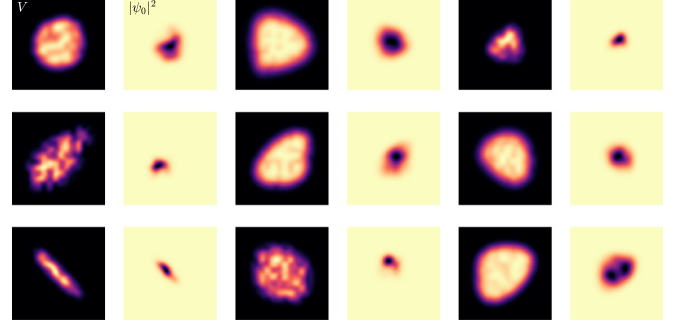
FIG. 10. Some example random potentials V and the norm of their associated ground-state wave functions $|\psi_0|^2$.

3. Double-well inverted Gaussians

The DIG potentials are generated with the scalar function

$$V(x,y) = -A_1 \exp\left[-\left(\frac{x - c_{x_1}}{k_{x_1}}\right)^2 - \left(\frac{y - c_{y_1}}{k_{y_1}}\right)^2\right]$$
$$- A_2 \exp\left[-\left(\frac{x - c_{x_2}}{k_{x_2}}\right)^2 - \left(\frac{y - c_{y_2}}{k_{y_2}}\right)^2\right], \quad \text{(B4)}$$

where the parameters are randomly sampled from a uniform distribution within the ranges given in Table II. These ranges were determined through trial and error to achieve energies in the range of 0–400 mHa.

4. Random potentials

The random potentials are generated through a lengthy process motivated by three requirements: The potentials must (a) be random (i.e., extremely improbable that two identical potentials ever be generated), (b) be smooth, and (c) go to a maximum of 20.0 at the boundary. First, we generate a 16×16
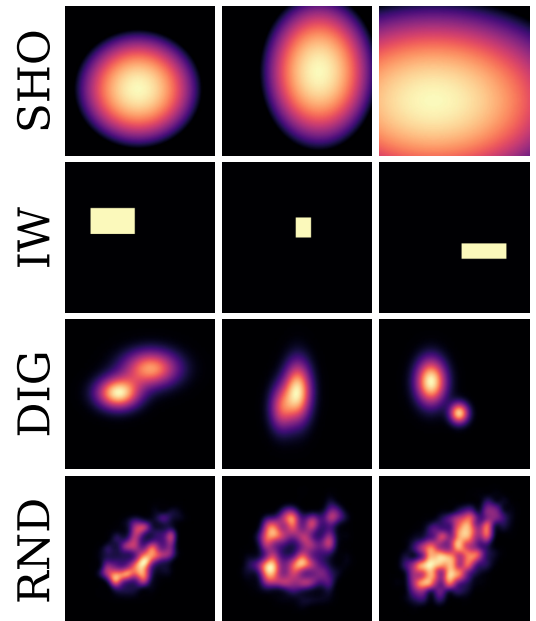

FIG. 11. Examples of the four classes of potentials.

binary grid of 1's and 0's and upscale it to 256×256. We then generate a second 16×16 binary grid and upscale it to 128×128. We center the smaller grid within the larger grid and then subtract them elementwise. We then apply a Gaussian blur with standard deviation σ_1 to the resulting image, where σ_1 is generated uniformly within the range given in Table III. The potential is now random and smooth, but does not achieve a maximum at the boundary.

To achieve this, we generate a mask that smoothly goes to 0 at the boundary and 1 in the interior. We wish the mask to be random, e.g., a randomly generated blob. To generate the blob, we generate k^2 random coordinate pairs on a 200×200 grid, where k is an integer between 2 and 7, inclusive. We then throw away all points that lie inside the convex hull of these points and smoothly interpolate the remaining points with cubic splines. We then form a binary mask by filling the inside of this closed blob with 1's and the outside with 0's. Resizing the blob to a resolution of $R \times R$ and applying a Gaussian blur with standard deviation σ_2, we arrive at the final mask. Here R and σ_2 are generated uniformly within the ranges given in Table III.

Elementwise multiplication of the mask with the randomly blurred image gives a random potential that approaches zero at the boundary. We randomize the "sharpness" of the potential by then exponentiating by $d = 0.1$, 0.5, 1.0, or 2.0, chosen at random with equal probabilities (i.e., $V := V^d$). We then subtract the result from its maximum to invert the well.

This process, while lengthy, produces very random potentials, of which no two are alike. The energy range of 0–400 mHa is appropriate for producing wave functions that span a moderate portion of the domain, as shown in Fig. 10. Examples of all classes of potentials can be seen in Fig. 11.

[1] P. A. M. Dirac, Proc. R. Soc. London Ser. A **123**, 714 (1929).

[2] M. J. Cherukara, B. Narayanan, A. Kinaci, K. Sasikumar, S. K. Gray, M. K. Chan, and S. K. R. S. Sankaranarayanan, J. Phys. Chem. Lett. **7**, 3752 (2016).

[3] M. Riera, A. W. Götz, and F. Paesani, Phys. Chem. Chem. Phys. **18**, 30334 (2016).

[4] A. Jaramillo-Botero, S. Naserifar, and W. A. Goddard, J. Chem. Theory Comput. **10**, 1426 (2014).

[5] B. W. H. van Beest, G. J. Kramer, and R. A. van Santen, Phys. Rev. Lett. **64**, 1955 (1990).

[6] J. W. Ponder and D. A. Case, Adv. Protein Chem. **66**, 27 (2003).

[7] V. Hornak, R. Abel, A. Okur, B. Strockbine, A. Roitberg, and C. Simmerling, Proteins **65**, 712 (2006).

[8] D. J. Cole, M. C. Payne, G. Csányi, S. Mark Spearing, and L. Colombi Ciacchi, J. Chem. Phys. **127**, 204704 (2007).

[9] J. D. van der Waals, De continuiteit van den gasen Vloeistoftoestand, Ph.D. thesis, University of Leiden, 1873.

[10] H. Z. Li, L. Li, Z. Y. Zhong, Y. Han, L. Hu, and Y. H. Lu, Math. Prob. Eng. **2013**, 860357 (2013).

[11] J. Behler and M. Parrinello, Phys. Rev. Lett. **98**, 146401 (2007).

[12] T. Morawietz and J. Behler, J. Phys. Chem. A **117**, 7356 (2013).

[13] J. Behler, R. Martonák, D. Donadio, and M. Parrinello, Phys. Status Solidi B **245**, 2618 (2008).

[14] P. E. Dolgirev, I. A. Kruglov, and A. R. Oganov, AIP Adv. **6**, 085318 (2016).

[15] N. Artrith and A. Urban, Comput. Mater. Sci. **114**, 135 (2016).

[16] W. Tian, F. Meng, L. Liu, Y. Li, and F. Wang, Sci. Rep. **7**, 40827 (2017).

[17] M. Rupp, A. Tkatchenko, K. R. Müller, and O. A. von Lilienfeld, Phys. Rev. Lett. **108**, 058301 (2012).

[18] F. A. Faber, L. Hutchison, B. Huang, J. Gilmer, S. S. Schoenholz, G. E. Dahl, O. Vinyals, S. Kearnes, P. F. Riley, and O. A. von Lilienfeld, J. Chem. Theory Comput. (2017), doi: 10.1021/acs.jctc.7b00577.

[19] G. Montavon, M. Rupp, V. Gobre, A. Vazquez-Mayagoitia, K. Hansen, A. Tkatchenko, K. R. Müller, and O. Anatole von Lilienfeld, New J. Phys. **15**, 095003 (2013).

[20] A. Lopez-Bezanilla and O. A. von Lilienfeld, Phys. Rev. B **89**, 235411 (2014).

[21] Y. Jia, E. Shelhamer, J. Donahue, S. Karayev, J. Long, R. Girshick, S. Guadarrama, and T. Darrell, arXiv:1408.5093.

[22] S. Curtarolo, D. Morgan, K. Persson, J. Rodgers, and G. Ceder, Phys. Rev. Lett. **91**, 135503 (2003).

[23] G. Hautier, C. C. Fischer, A. Jain, T. Mueller, and G. Ceder, Chem. Mater. **22**, 3762 (2010).

[24] Y. Saad, D. Gao, T. Ngo, S. Bobbitt, J. R. Chelikowsky, and W. Andreoni, Phys. Rev. B **85**, 104104 (2012).

[25] L. Wang, Phys. Rev. B **94**, 195105 (2016).

[26] C. Monterola and C. Saloma, Opt. Commun. **222**, 331 (2003).

[27] Y. Shirvany, M. Hayati, and R. Moradian, Commun. Nonlinear Sci. Numer. Simul. **13**, 2132 (2008).

[28] C. Caetano, J. L. Reis, J. Amorim, M. R. Lemes, and A. D. Pino, Int. J. Quantum Chem. **111**, 2732 (2011).

[29] B. P. van Milligen, V. Tribaldos, and J. A. Jiménez, Phys. Rev. Lett. **75**, 3594 (1995).

[30] G. Carleo and M. Troyer, Science **355**, 602 (2017).

[31] J. C. Snyder, M. Rupp, K. Hansen, K.-R. Müller, and K. Burke, Phys. Rev. Lett. **108**, 253002 (2012).

[32] F. Brockherde, L. Vogt, L. Li, M. E. Tuckerman, K. Burke, and K.-R. Müller, arXiv:1609.02815.

[33] K. Yao and J. Parkhill, J. Chem. Theory Comput. **12**, 1139 (2016).

[34] Y. LeCun, L. Bottou, Y. Bengio, and P. Haffner, Proc. IEEE **86**, 2278 (1998).

[35] P. Simard, D. Steinkraus, and J. Platt, in *Proceedings of the Seventh International Conference on Document Analysis and Recognition* (IEEE, Piscataway, 2003), Vol. 1, pp. 958–963.

[36] D. C. Ciresan, U. Meier, J. Masci, L. M. Gambardella, and J. Schmidhuber, in *Proceedings of the 22nd International Joint Conference on Artificial Intelligence* (AAAI, Palo Alto, 2011), Vol. 22, pp. 1237–1242.

[37] C. Szegedy, W. Liu, Y. Jia, P. Sermanet, S. Reed, D. Anguelov, D. Erhan, V. Vanhoucke, and A. Rabinovich, in *Proceedings of the IEEE Computer Society Conference on Computer Vision and Pattern Recognition* (IEEE, Piscataway, 2015), pp. 1–9.

[38] D. Silver, A. Huang, C. J. Maddison, A. Guez, L. Sifre, G. van den Driessche, J. Schrittwieser, I. Antonoglou, V. Panneershelvam, M. Lanctot, S. Dieleman, D. Grewe, J. Nham, N. Kalchbrenner, I. Sutskever, T. Lillicrap, M. Leach, K. Kavukcuoglu, T. Graepel, and D. Hassabis, Nature (London) **529**, 484 (2016).

[39] V. Mnih, K. Kavukcuoglu, D. Silver, A. A. Rusu, J. Veness, M. G. Bellemare, A. Graves, M. Riedmiller, A. K. Fidjeland, G. Ostrovski, S. Petersen, C. Beattie, A. Sadik, I. Antonoglou, H. King, D. Kumaran, D. Wierstra, S. Legg, and D. Hassabis, Nature (London) **518**, 529 (2015).

[40] K. I. Funahashi, Neural Networks **2**, 183 (1989).

[41] J. L. Castro, C. J. Mantas, and J. M. Benítez, Neural Networks **13**, 561 (2000).

[42] A. Krizhevsky, I. Sutskever, and G. E. Hinton, in *Proceedings of the 25th International Conference on Neural Information Processing Systems* (Curran, Red Hook, 2012), pp. 1097–1105.

[43] D. H. Hubel and T. N. Wiesel, J. Physiol. **195**, 215 (1968).

[44] Y. Bengio, Found. Trends Mach. Learn. **2**, 1 (2009).

[45] P. Mehta and D. J. Schwab, arXiv:1410.3831.

[46] H. W. Lin, M. Tegmark, and D. Rolnick, J. Stat. Phys. **168**, 1223 (2017).

[47] K. T. Schütt, F. Arbabzadah, S. Chmiela, K. R. Müller, and A. Tkatchenko, Nat. Commun. **8**, 13890 (2017).

[48] P. Frolkovič, *Acta Applicandae Mathematicae*, 3rd ed. (Cambridge University Press, New York, 1990), Vol. 19, pp. 297–299.

[49] A. Gharaati and R. Khordad, Superlatt. Microstruct. **48**, 276 (2010).

[50] S. S. Gomez and R. H. Romero, Cent. Eur. J. Phys. **7**, 12 (2009).

[51] M. D. Zeiler, arXiv:1212.5701.

[52] M. Abadi *et al.*, arXiv:1603.04467 (2015).

[53] L. F. Arsenault, A. Lopez-Bezanilla, O. A. von Lilienfeld, and A. J. Millis, Phys. Rev. B **90**, 155136 (2014).

[54] L. Li, J. C. Snyder, I. M. Pelaschier, J. Huang, U.-N. Niranjan, P. Duncan, M. Rupp, K.-R. Müller, and K. Burke, Int. J. Quantum Chem. **116**, 819 (2016).

[55] T. Suzuki, R. Tamura, and T. Miyazaki, Int. J. Quantum Chem. **117**, 33 (2017).

[56] L. Ward, A. Agrawal, A. Choudhary, and C. Wolverton, Npj Comp. Mat. **2**, 16028 (2016).

[57] S. Kearnes, K. McCloskey, M. Berndl, V. Pande, and P. Riley, J. Comput.-Aided Mol. Des. **30**, 595 (2016).

[58] S. Dieleman, K. W. Willett, and J. Dambre, Mon. Not. R. Astron. Soc. **450**, 1441 (2015).

[59] D. E. Worrall, S. J. Garbin, D. Turmukhambetov, and G. J. Brostow, arXiv:1612.04642.

[60] S. Dieleman, J. De Fauw, and K. Kavukcuoglu, arXiv:1602.02660.

[61] W. Kohn, Int. J. Quantum Chem. **56**, 229 (1995).

[62] S. A. Kucharski and R. J. Bartlett, J. Chem. Phys. **97**, 4282 (1992).

[63] F. Pedregosa, G. Varoquaux, A. Gramfort, V. Michel, B. Thirion, O. Grisel, M. Blondel, G. Louppe, P. Prettenhofer, R. Weiss, V. Dubourg, J. Vanderplas, A. Passos, D. Cournapeau, M. Brucher, M. Perrot, and É. Duchesnay, J. Mach. Learn. Res. **12**, 2825 (2011).